IAC-06-C1.8.01

CONTROL OF SATELLITE IMAGING FORMATIONS IN MULTI-BODY REGIMES

Kathleen C. Howell
Hsu Lo Professor of Aeronautical and Astronautical Engineering
School of Aeronautics and Astronautics
Purdue University
West Lafayette, Indiana
howell@purdue.edu

Lindsay D. Millard
Graduate Student
School of Aeronautics and Astronautics
Purdue University
West Lafayette, Indiana
lmillard@purdue.edu

ABSTRACT

Libration point orbits may be ideal locations for satellite imaging formations. Therefore, control of these arrays in multi-body regimes is critical. A continuous feedback control algorithm is developed that maintains a formation of satellites in motion that is bounded relative to a halo orbit. This algorithm is derived based on the dynamical characteristics of the phase space near periodic orbits in the circular restricted three-body problem (CR3BP). By adjusting parameters of the control algorithm appropriately, satellites in the formation follow trajectories that are particularly advantageous to imaging arrays. Image reconstruction and coverage of the (u, v) plane are simulated for interferometric satellite configurations, demonstrating potential applications of the algorithm and the resulting motion.

INTRODUCTION

Satellite imaging formations have numerous applications in the future of space exploration. These include: searches for exosolar planets, identification of black holes, and spectral characterization of distant stars. Libration point orbits may be ideal locations for such imaging arrays.[1,2,3] Therefore, control of these arrays in multi-body regimes is critical.

Much of the available research in formation flight applications focuses on Earth orbiting configurations, where the influence of other gravitational perturbations can be safely ignored.[4,5] However, interest in formations that evolve near the vicinity of the Sun-Earth libration points has inspired new studies regarding formation keeping in the three-body problem.[6-12] Howell and Marchand consider linear optimal control, as applied to nonlinear time-varying systems, as well as nonlinear control techniques, including input and output feedback linearization.[13] These control strategies are applied to a two spacecraft formation where the chief spacecraft evolves along a three-dimensional periodic halo orbit near the L2 libration point. In a later work, the control strategies are shown to be effective in the full ephemeris model.[14] Howell and Barden investigate formation flying in the vicinity of the libration points in the CR3BP. Initially, their focus is the determination of the natural behavior on the center manifold near the libration points. The first stage of their study captures a naturally occurring six-satellite formation near the libration points.[15,16] Further analysis considered strategies to maintain a periodic, planar formation of the six vehicles in an orbit about the Sun-Earth L1 point.[17,18] The deviation of each spacecraft is controlled impulsively relative to the plane of the initial formation, one that is specified to be contained within the center manifold. The natural flow in the center subspace is such that the relative distances between each spacecraft remain essentially bounded and the relative configuration of the formation is time independent. Marchand and Howell extend this analysis by revealing other potentially interesting nominal motions as well as discrete control strategies for deployment and station-keeping.[19]

Research in the specific area of interferometric satellite formation control has been pursued, but only in limited scope. Different methods have been explored to determine satellite motion that minimizes fuel while attaining an adequately resolute image. Chakravorty develops a model for the process of image formation in a multi-spacecraft interferometric system.[20,21] Hyland extends this model to formulate an image-quality based figure of merit for optimal control strategies.[22,23] Hussein, Scheeres, and Hyland identify a special class of two-dimensional spiral motions that satisfy the necessary imaging requirements for certain interferometric imaging missions. Isolation of this class of motion serves as a basis for the identification of a relationship between image quality and fuel expenditure. The spacecraft are assumed to be moving in free space; the only forces acting on the system are control forces.[24,25] Hussein et al. expand this analysis by formulating an optimal control problem to minimize measurement noise and fuel while maximizing certain image metrics. Although the two-point boundary value problem remains unsolved,

necessary conditions for optimality are defined and these reveal the general behavior of an optimal solution. Again, the spacecraft are assumed to be moving in free space.[26,27] Finally, Hussein and Bloch apply dynamic coverage optimal control (a geometric control method) to interferometric imaging arrays. However, the formulation incorporates assumptions that include: a system that evolves only on planar or paraboloidal Riemannian manifolds and is not evolving in any gravitational field.[28,29]

The goal in the present investigation is the development of a feedback control algorithm that maintains a given number of satellites within some bounded region relative to a halo orbit. This algorithm is developed based on the dynamical characteristics of the phase space near periodic orbits in the CR3BP. By adjusting parameters of the control algorithm appropriately, trajectories that are particularly advantageous to optical formations emerge. Image reconstruction and coverage of the (u, v) plane are simulated for interferometric satellite formations, demonstrating potential applications of the algorithm and resulting motion.

OPTICS

The resolution of an image produced by an interferometric satellite array is largely determined by the corresponding coverage of the (u,v) plane. In turn, coverage of the (u, v) plane is derived based on several characteristics of the satellite configuration and motion in physical space. Therefore, to determine the formation motion that may be advantageous to imaging, a mathematical model relating satellite motion in physical space to coverage of the (u, v) plane, and thus image reconstruction, is necessary.

Background

A light beam is an electromagnetic wave propagating through space. This electromagnetic wave is composed of an oscillating electric field and an oscillating magnetic field; these fields are perpendicular to each other and to the direction of propagation of the wave. The electric field, $F(t, z)$, associated with a linearly polarized, plane electromagnetic wave traveling in the positive z direction at a time t is modeled as follows,

$$F(t,z) \equiv a_m \cos\left(2\pi f t - \frac{2\pi}{\lambda} z\right) \equiv a_m \cos(\omega t - k z) \qquad [1]$$

The value f [cycles/sec] is the temporal frequency of the oscillating electric field, the value λ [meters] is the spatial wavelength of the oscillating electric field, and a_m is the maximum amplitude [Newtons/Coulomb] of the oscillating electric field. Alternatively, the traveling wave is written in terms of the wave number, k, and the angular frequency, ω.

As a result of the extremely high frequencies (short wavelengths) of light waves, the human eye cannot detect the oscillations of the electric field at a particular point. Instead, the eye inherently performs a time averaging. Consider a unit surface area perpendicular to a plane electromagnetic wave; then, the rate at which energy flows through the surface area at a given time, t, is evaluated as

$$R(t) = \frac{a_m^2}{\mu_0 c} \cos^2(2\pi f t - k z) \qquad [2]$$

where μ_0 is the constant of permeability of free space (4π x 10^{-7} N/A/A) and c is the speed of light in a vacuum (3 x 10^8 m/s). The time average of $R(t)$ is called *light intensity*. This is the quantity that is detectable by the human eye. This time average is represented by the following expression,

$$I \equiv R_{avg} = \lim_{T\to\infty} \frac{1}{2T} \int_{-T}^{T} \frac{a_m^2}{\mu_0 c} \cos^2(k z - 2\pi f t)\, dt = \frac{a_m^2}{2\mu_0 c} \qquad [3]$$

The intensity of a linearly polarized plane electromagnetic wave is relatively easy to describe analytically; the intensity of an incoherent light source is much more complicated. Most stars and planets are considered *extended incoherent light sources*, or a collection of electromagnetic waves of known frequencies that are constantly changing phase and amplitude in a random fashion. For an incoherent light source, I is not a constant. Instead, it is a function of two variables that define the average light intensity at each location on the image plane, and possibly time. In that case, I is often termed the *irradiance pattern* or *image* of the incoherent source. At any given time, it is impossible to predict the amplitude or the phase of a light wave produced by an extended incoherent source.

In 1938 and 1939, respectively, P.H. van Cittert and F. Zernike proved that the irradiance pattern (image) of an extended incoherent source is related to the Fourier transform of a function called the complex mutual coherence function. This result is the basis for interferometric imaging.

Consider the situation depicted in Figure 1. A celestial body, S, is emitting incoherent light from some point in space. This source is approximately located in a two-dimensional plane, at some long distance, z, from the observation point. The *source plane* is denoted with an (x, y) coordinate frame. A spacecraft interferometer is located in the *observation plane*, labeled with an (v, η) coordinate frame. Two apertures, that collect light photons, are located within the observation plane. These two apertures are located at points (v_1, η_1) and (v_2, η_2). The goal is to construct the irradiance pattern (image), $I(x, y)$, of S with measurements of the light source in the (v, η) plane.

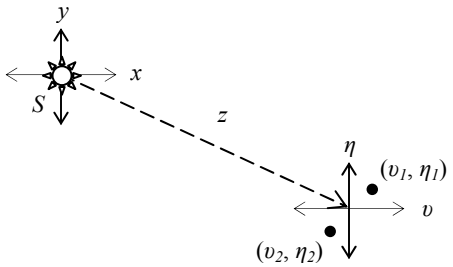

Figure 1: Interferometric imaging architecture.

From the van Cittert-Zernike result,

$$I(x,y) \cong \int_u \int_v \mu(u,v) e^{i2\pi(ux+vy)} dvdu \qquad [4]$$

where $I(x, y)$ is the image of the source S and the quantities u and v are defined as

$$u \equiv \frac{\eta_1 - \eta_2}{z\lambda} \qquad [5]$$

$$v \equiv \frac{\upsilon_1 - \upsilon_2}{z\lambda} \qquad [6]$$

Then, $\mu(x, y)$ is the complex mutual coherence function and λ is defined as the wavelength of emitted light.

From equation [4], it is apparent that the image is constructed from μ and therefore, depends on both u and v. In turn, u and v are functions of the relative locations of the satellite apertures in physical space. The (u, v) plane, however, is not a physical plane. Rather, it is constructed from the relative distances of one aperture with respect to the other. In reality, the interferometer will *not* be located in a plane perpendicular to the line of sight to the object of interest. Thus, motion of the apertures is generally projected onto this perpendicular plane.

The van Cittert-Zernike result implies that if the value of the complex mutual coherence function is known at every point in the (u, v) plane, a two-dimensional Fourier transform may be used to create an image. The two-dimensional Fourier transform is expressed as,

$$I(x,y) \equiv \int_{-\infty}^{\infty} \int_{-\infty}^{\infty} \mu(u,v) e^{i2\pi(ux+vy)} dudv \qquad [7]$$

Fourier series representations are associated with periodic signals. However, in the limit, a Fourier series leads to a Fourier transform. Then,

$$I(x,y) \equiv \int_{-\infty}^{\infty} \int_{-\infty}^{\infty} \mu(u,v) e^{i2\pi(ux+vy)} dudv = \lim_{u_0, v_0 \to 0} \sum_{n=-\infty}^{\infty} \sum_{m=-\infty}^{\infty} \mu_{n,m} e^{i2\pi(nu_0 x + mv_0 y)} \qquad [8]$$

where u_0 and v_0 are fundamental spatial frequencies [cycles/unit length]. A real, periodic, two-dimensional signal can be represented by[30]

$$I(x,y) = \mu_{0,0} + \lim_{u_0, v_0 \to 0} \sum_{n=-\infty}^{\infty} \sum_{m=-\infty}^{\infty} 2\text{Real}\left(\mu_{n,m} e^{i2\pi(nu_0 x + mv_0 y)}\right) \qquad [9]$$

The complex Fourier coefficient, μ_{nm}, can be written in polar form,

$$\mu_{nm} = A_{nm} e^{i\theta_{nm}} \qquad [10]$$

where A_{nm} is the amplitude of the Fourier coefficient and θ_{nm} is the phase. Then,

$$I(x,y) = \mu_{0,0} + 2\sum_{n=1}^{\infty} \sum_{m=1}^{\infty} A_{nm} \cos\left(2\pi(nu_0 x + mv_0 y) + \theta_{nm}\right) \qquad [11]$$

The two-dimensional (2D) cosine function is the basic building block of the image. The 2D cosine function possesses two different frequencies, one in the x direction, i.e., $u \equiv nu_0$, and one in the y direction, $v \equiv mv_0$. These are spatial frequencies represented in [cycles/unit length]. Any real 2D image may be created by superimposing (in space) an infinite number of 2D cosine functions. Therefore, every value of the mutual coherence function in the (u, v) plane corresponds to one 2D cosine function. Furthermore, the complex mutual coherence function at a point in the (u, v) plane is equivalent to a complex Fourier coefficient, which defines the amplitude and phase at each spatial frequency.[31]

Simulating Image Reconstruction

To simulate interferometric image reconstruction, a digitized monochromatic picture is selected to represent the *actual* image. In practice, the "actual image" is the irradiance pattern if an infinite number of measurements in the (u, v) plane are possible. The simulated image is constructed as a matrix of numbers between zero and one, with each number representing a different shade of the image color. For example, Figure 2 is comprised of 200 x 200 pixels. It is represented by a 200 x 200 matrix with entries varying between zero and one, depending on the shade of the individual pixel. Since interferometric imaging is being

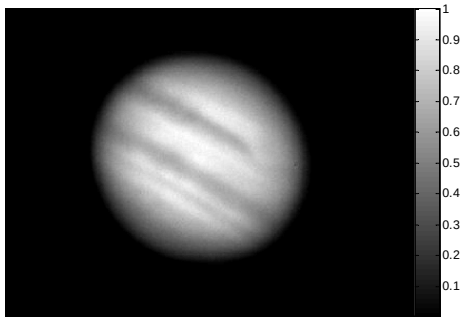

Figure 2: Digitized monochromatic picture is the "true" image of the observed planet.

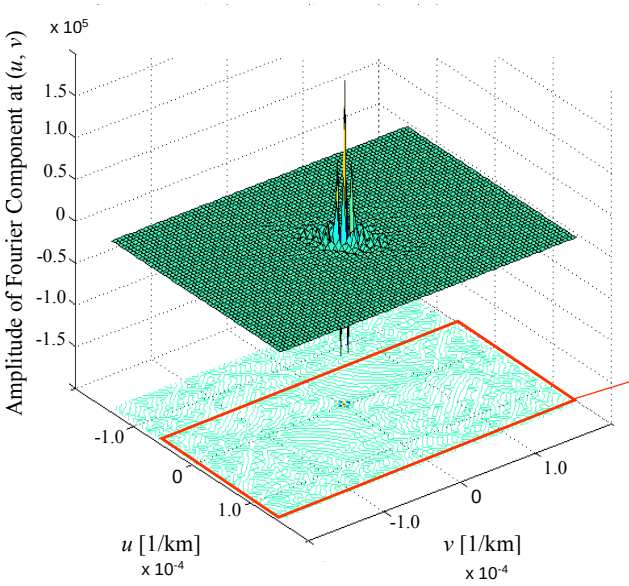

Figure 3: Two-Dimensional Fast Fourier Transform of Actual Image

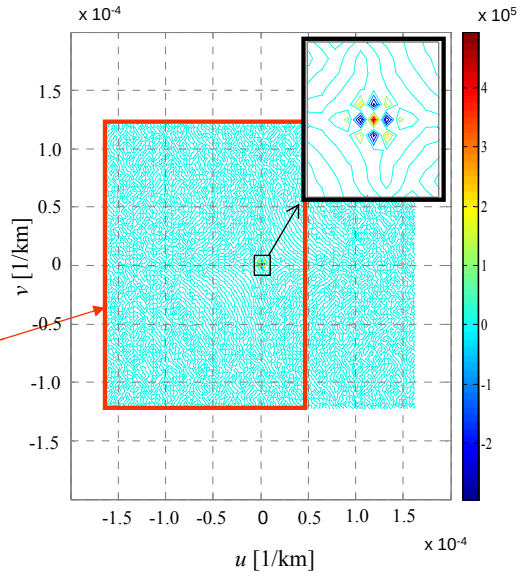

Figure 4: Contour Plot of Mutual Coherence Function on the (u, v) Plane

simulated numerically (thus, the actual image has a finite number of pixels), only a finite number of well-placed measurements are required to completely and accurately reconstruct the image. In reality, an infinite number of measurements are necessary in order to completely reconstruct the actual image.

Next, a two-dimensional Fast Fourier Transform (FFT) of this image matrix is computed numerically. The FFT provides the Fourier amplitude associated with each combination of spatial frequencies in the image. In other words, the 2D FFT is the mutual coherence function of the "actual image." Plots of these amplitudes as a function of the spatial frequencies, u and v, appear in Figures 3 and 4. An interferometer can measure the mutual coherence function at different locations in the (u, v) plane. These locations in the (u, v) plane are determined by the distance between the spacecraft in the interferometric array, the number of spacecraft, the motion of the individual spacecraft, the distance to the object being observed, and the wavelength of light being observed. From equations [5] and [6], a relationship between the locations of spacecraft in physical space and specific points on the (u, v) plane is described. Of course, it requires two spacecraft, or a *baseline*, moving in physical space to yield points on the (u, v) plane. As more and more points on the (u, v) plane are measured (more and more Fourier amplitudes are obtained) the reconstructed mutual coherence function approaches the actual mutual coherence function and the image becomes more resolute, as is apparent in Figure 5.

The amplitudes of the Fourier component, when u and v are small, are very large. These amplitudes correspond to the coarse features of the image. When u and v are large, the Fourier component is small, corresponding to finer features in the image.

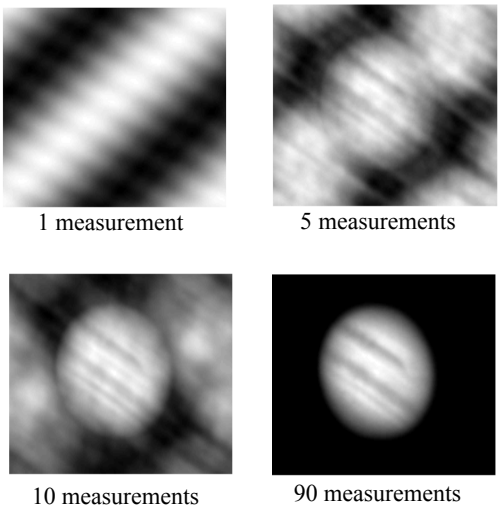

Figure 5. The reconstructed image approaches the actual Image as more points in the (u, v) plane are measured.

DYNAMICAL MODEL: CR3BP

The motion of a particle (spacecraft) in the CR3BP is described in terms of rotating coordinates relative to the barycenter of the system primaries. For this analysis, focus is placed on formations near the libration points in the Sun-Earth/Moon system, since these tend to be the most advantageous for interferometric imaging. In this frame, the rotating *x*-axis is directed from the Sun towards the Earth-Moon barycenter. The *z*-axis is normal to the plane of motion of the primaries, and the *y*-axis completes the right-handed triad. The general non-dimensional equations of motion, relative to the system barycenter, are of the form:

$$\ddot{x} - 2\dot{y} - x = -\frac{(1-\mu_G)(x+\mu_G)}{r_1^3} - \frac{\mu_G(x-(1-\mu_G))}{r_2^3} \quad [12]$$

$$\ddot{y} + 2\dot{x} - y = -\frac{(1-\mu_G)y}{r_1^3} - \frac{\mu_G y}{r_2^3} \quad [13]$$

$$\ddot{z} = -\frac{(1-\mu_G)z}{r_1^3} - \frac{\mu_G z}{r_2^3} \quad [14]$$

where

$$r_1 = \left((x+\mu_G)^2 + y^2 + z^2\right)^{1/2} \quad [15]$$

$$r_2 = \left((x-(1-\mu_G))^2 + y^2 + z^2\right)^{1/2} \quad [16]$$

The quantity μ_G is a non-dimensional mass parameter associated with the system. For the Sun-Earth system, $\mu_G \approx 3.0404 \times 10^{-6}$. A more compact notation incorporates a pseudo-potential function, *U*, such that

$$U = \frac{(1-\mu_G)}{r_1} + \frac{\mu_G}{r_2} + \frac{1}{2}\left(x^2 + y^2\right) \quad [17]$$

Then, the scalar equations of motion are rewritten in the form

$$\ddot{x} - 2\dot{y} = U_x \quad [18]$$

$$\ddot{y} + 2\dot{x} = U_y \quad [19]$$

$$\ddot{z} = U_z \quad [20]$$

where the symbol U_j denotes $\frac{\partial U}{\partial j}$. Equations [13]-[15] or equations [19]-[21] comprise the dynamical model in the circular restricted three-body problem.

Given a solution to the nonlinear differential equations, linear variational equations of motion in the CR3BP can be derived as

$$\dot{\delta\bar{X}}(t) = A(t)\,\delta\bar{X}(t) \quad [21]$$

where $\delta\bar{X}(t) \equiv [\delta x \;\; \delta y \;\; \delta z \;\; \delta\dot{x} \;\; \delta\dot{y} \;\; \delta\dot{z}]^T$ represents variations with respect to a reference trajectory. Generally, the reference solutions of interest are not constant. In this analysis, the reference trajectory is periodic. In particular, the focus of this work is the family of periodic halo orbits. Thus, *A(t)* is periodic and time-varying, of the form

$$A(t) = \begin{bmatrix} 0 & 0 & 0 & 1 & 0 & 0 \\ 0 & 0 & 0 & 0 & 1 & 0 \\ 0 & 0 & 0 & 0 & 0 & 1 \\ U_{xx} & U_{xy} & U_{xz} & 0 & 2 & 0 \\ U_{yx} & U_{yy} & U_{yz} & -2 & 0 & 0 \\ U_{zx} & U_{zy} & U_{zz} & 0 & 0 & 0 \end{bmatrix} \quad [22]$$

The partials U_{kl} are also functions of time, although the functional dependence on time, *t*, has been dropped.

The general form of the solution to the system in equation [21] is

$$\delta\bar{X}(t) = \Phi(t,t_0)\,\delta\bar{X}(t_0) \quad [23]$$

where $\Phi(t,t_0)$ is the state transition matrix (STM). The STM is a linear map from the initial state at the initial time t_0 to a state at some later time *t*, and, thus, offers an approximation of the impact of the variations in the initial state on the evolution of the trajectory. The STM must satisfy the matrix differential equation

$$\dot{\Phi}(t,t_0) = A(t)\,\Phi(t,t_0) \quad [24]$$

given the initial condition,

$$\Phi(t_0,t_0) = \mathrm{I}_6 \quad [25]$$

where I_6 is the 6×6 identity matrix.

It is clear that the STM at time *t* can be numerically determined by integrating equation [24] from the initial value. Since the STM is a 6×6 matrix, propagation of equations [24] and [25] requires the integration of 36 first-order, scalar, differential equations. Since the elements of *A(t)* depend on the reference trajectory, equation [24] must be integrated simultaneously with the nonlinear equations of motion to generate reference states. This necessitates the integration of an additional 6 first-order equations, for a total of 42 differential equations.

CONTINUOUS FLOQUET CONTROL

Derivation of the Control Law

The main result from Floquet is that, for a time-varying, periodic, linear system, the STM can be factored into two matrices, *E* and *J*, in the form

$$\Phi(t,0) = E(t)\,e^{Jt}\,E^{-1}(0) \quad [26]$$

The matrix *J* is a constant matrix, usually in the Jordan normal form. Its diagonal entries, ω_i are the Poincaré exponents, the analog of the eigenvalues for constant-coefficient systems. The matrix *E(t)* is periodic with the same period, *T*, as the original system in equation [21].

Solving a Floquet problem for all time thus requires the determination of the constant matrix J and the periodic matrix $E(t)$ over one period.

Since the matrix E is periodic, $E(0) = E(T)$ and, at $t = T$, equation [26] becomes

$$\Phi(T,0) = E(0)\, e^{JT} E^{-1}(0) \qquad [27]$$

Thus, $E(0)$ is the matrix of eigenvectors of the monodromy matrix, $\Phi(t, t_0)$. The eigenvalues of the monodromy matrix, λ_i, are related to the Poincaré exponents ω_i, i.e.,

$$\lambda_i = e^{\omega_i T} \qquad [28]$$

After numerically integrating equation [24] over one period, the Poincaré exponents and the eigenvector matrix at $t = 0$ can be obtained. Since $E(t)$ is periodic, and therefore bounded, the stability of the system is governed by ω_i (or λ_i) alone.

The reference trajectory, or halo orbit, of interest is inherently unstable. In fact, the six-dimensional eigenstructure of the monodromy matrix is characterized by one unstable eigenvalue (λ_1), one stable eigenvalue (λ_2), and four eigenvalues in the center subspace. Two of these neutrally stable eigenvalues are located on the unit circle (λ_3 and λ_4) and the remaining two are exactly equal to one (λ_5 and λ_6).

At any point in time, the perturbation $\delta\bar{X}(t)$ can be expressed in terms of any six-dimensional basis. The Floquet modes ($\bar{e}_j$), defined by the columns of $E(t)$, form a non-orthogonal six-dimensional basis. Hence,

$$\delta\bar{X}(t) = \sum_{j=1}^{6} \delta\bar{X}_j(t) = \sum_{j=1}^{6} c_j(t)\,\bar{e}_j(t) \qquad [29]$$

where $\delta\bar{X}_j(t)$ denotes the component of $\delta\bar{X}(t)$ along the j^{th} mode, $\bar{e}_j(t)$, and the coefficients $c_j(t)$ are determined as the elements of the vector $\bar{c}(t)$ defined by

$$\bar{c}(t) = E(t)^{-1}\,\delta\bar{X}(t) \qquad [30]$$

This Floquet structure is implemented by Gómez et al.[11] and later by Howell and Keeter[32] as the basis of a station keeping strategy for a single spacecraft evolving along a halo orbit. Both investigations determine the impulsive maneuver scheme that is required to remove the component in the direction of the unstable mode $\delta\bar{X}_1$ (as defined in [29]), of the perturbation $\delta\bar{X}(t)$ at discrete intervals. For instance, let

$$\delta\bar{X}_{desired}(t) = \sum_{j=2}^{6} \left(1 + \alpha_j(t)\right)\delta\bar{X}_j(t) \qquad [31]$$

denote the desired perturbation relative to the reference orbit, where the $\bar{\alpha}(t)$ is some, yet to be determined, coefficient vector. Note that the limits of the summation range from 2 through 6 which implies that the perturbation in the direction of the unstable mode $\bar{e}_1$ has been removed. The linearized control problem then reduces to computing the impulsive maneuver, $\Delta\bar{v}(t)$, such that

$$\sum_{j=2}^{6} \left(1 + \alpha_j(t)\right)\delta\bar{X}_j(t) = \sum_{k=1}^{6} \delta\bar{X}_k(t) + \begin{bmatrix} 0_{3x1} \\ \Delta\bar{v}(t)_{3x1} \end{bmatrix} \qquad [32]$$

After some reduction, equation [32] can be rewritten in matrix form as

$$\begin{bmatrix} \delta\bar{X}_2(t) & \delta\bar{X}_3(t) & \delta\bar{X}_4(t) & \delta\bar{X}_5(t) & \delta\bar{X}_6(t) & \begin{matrix} 0_{3x3} \\ -I_{3x3} \end{matrix} \end{bmatrix} \times \begin{bmatrix} \bar{\alpha}(t)_{5x1} \\ \Delta\bar{v}(t)_{3x1} \end{bmatrix} = \delta\bar{X}_1(t) \qquad [33]$$

where $\bar{\alpha}$ represents a 5 x 1 vector formed by the α_j components in equation [32]. Therefore, the maneuver, $\Delta\bar{v}_{3x1}$, that is required to remove the unstable mode $\bar{e}_1$ from the perturbation at any given time can be approximated from equation [33]. Howell and Keeter identify this required $\Delta\bar{v}_{3x1}$ via a minimum norm solution. If the maneuver is constrained to the Sun-Earth line ($\hat{x}$ - direction), $\Delta\bar{v}_{1x1}$ is actually a scalar, and the system possesses an exact solution.

If exactly three modes are removed and control is possible in three directions, the system also possesses an exact solution. For example, Marchand and Howell demonstrate the impulsive $\Delta\bar{v}(t)_{3x1}$ that is required to remove the portion of the perturbation along modes $\bar{e}_1$, $\bar{e}_3$, and $\bar{e}_4$. It can be determined exactly from

$$\begin{bmatrix} \bar{\alpha}(t)_{3x1} \\ \Delta\bar{v}(t)_{3x1} \end{bmatrix} = \begin{bmatrix} \delta\bar{X}_2(t) & \delta\bar{X}_5(t) & \delta\bar{X}_6(t) & \begin{matrix} 0_{3x3} \\ -I_{3x3} \end{matrix} \end{bmatrix}^{-1} \times \left(\delta\bar{X}_1(t) + \delta\bar{X}_3(t) + \delta\bar{X}_4(t)\right) \qquad [34]$$

Similary, the $\Delta\bar{v}_{3x1}$ vector that is required to remove modes $\bar{e}_1$, $\bar{e}_5$, and $\bar{e}_6$ is exactly determined from

$$\begin{bmatrix} \bar{\alpha}(t)_{3x1} \\ \Delta\bar{v}(t)_{3x1} \end{bmatrix} = \begin{bmatrix} \delta\bar{X}_2(t) & \delta\bar{X}_3(t) & \delta\bar{X}_4(t) & \begin{matrix} 0_{3x3} \\ -I_{3x3} \end{matrix} \end{bmatrix}^{-1} \times \left(\delta\bar{X}_1(t) + \delta\bar{X}_5(t) + \delta\bar{X}_6(t)\right) \qquad [35]$$

As formulated in [34] and [35], $\Delta\bar{v}(t)_{3x1}$ is the impulsive control necessary to remove perturbations in the direction of one unstable mode and two semi-stable modes in the linearized system represented in equation [21] at a given time. This methodology can be applied in a linear time-varying feedback loop,

$$\dot{\delta\bar{X}}(t) = A(t)\,\delta\bar{X}(t) + Bu(t) = A(t)\,\delta\bar{X}(t) + \begin{bmatrix} 0_{3x1} \\ \Delta\bar{v}(t)_{3x1} \end{bmatrix} \qquad [36]$$

$$\bar{Y}(t) = C\,\delta\bar{X}(t) \qquad [37]$$

where $B = [0_{3\times3}\ \ I_{3\times3}]^T$, indicating that the control input can instantaneously change only the velocity of the

satellite (not position) and $C = I_6$, implying full state feedback.

Stability of the Controlled Linear System

In the linearized system of the variational equations, the Floquet result can be applied to transform the time-varying periodic linear system in equation [21] to a time-*invariant* linear system.[33,34,35] The transformation proceeds as follows,

Initial system: $\dot{\delta\bar{X}}(t) = A(t)\delta\bar{X}(t)$

Coordinate Transformation: $\delta\bar{X}(t) = E(t)\bar{Z}(t)$ [38]

Resulting system: $\dot{\bar{Z}}(t) = J\,\bar{Z}(t)$ [39]

It is important to note that *E(t)* is the periodic Floquet modal matrix and *J* is the constant Floquet matrix containing the Poincaré exponents. Thus both *J* and *E(t)* are bounded and invertible. Addition of a state feedback loop to the initial system as in equation [36], then completing the transformation using equation [38], yields the following

Feedback system:

$$\dot{\delta\bar{X}}(t) = A(t)\delta\bar{X}(t) + Bu(t) = \left[A(t) + B\kappa(t)\right]\delta\bar{X}(t) \quad [40]$$
$$\bar{Y}(t) = C\,\delta\bar{X}(t)$$

Coordinate transformation: $\delta\bar{X}(t) = e(t)\bar{Z}(t)$

Resulting system:

$$\dot{\bar{Z}}(t) = \left[J + E(t)^{-1}B\kappa(t)E(t)\right]\bar{Z}(t) \quad [41]$$
$$\bar{W}(t) = CE(t)\bar{Z}(t) \quad [42]$$

where $\kappa(t)$ is some yet to be determined control effort. Let Q be the Jordan canonical form of J, where $Q = SJS^{-1}$. Then application of another transformation, yields

Feedback system: $\dot{\bar{Z}}(t) = \left[J + E(t)^{-1}Bk(t)E(t)\right]\bar{Z}(t)$
$\bar{W}(t) = CE(t)\bar{Z}(t)$

Coordinate transformation: $\bar{Z}(t) = S^{-1}\Gamma(t)$ [43]

Resulting system:

$$\dot{\bar{\Gamma}}(t) = \left[Q + SE(t)^{-1}Bk(t)E(t)S^{-1}\right]\bar{\Gamma}(t) \quad [44]$$
$$\bar{\Psi}(t) = CE(t)S^{-1}\bar{\Gamma}(t) \quad [45]$$

The diagonal entries of *Q* are now the Poincaré exponents corresponding to the system monodromy matrix. The system can be simplified by renaming some variables:

$$\dot{\bar{\Gamma}}(t) = \left[Q + g(t)w(t)\right]\bar{\Gamma}(t) \quad [46]$$
$$\bar{\Psi}(t) = h(t)\bar{\Gamma}(t) \quad [47]$$

where $g(t) = SE(t)^{-1}B$, $w(t) = \kappa(t)E(t)S^{-1}$, and $h(t) = CE(t)S^{-1}$. Because of the form of the Q matrix, the system is partitioned into modes that will be controlled (unstable and semi-stable modes) and modes that will be ignored (stable and semi-stable modes). This is accomplished via simple row operations that do not change the system. A partitioned system results,

$$w(t) = \begin{bmatrix} w_c(t) & w_i(t) \end{bmatrix} \quad [48]$$

$$g(t) = \begin{bmatrix} g_c(t) \\ g_i(t) \end{bmatrix} \quad [49]$$

$$Q = \begin{bmatrix} Q_C & 0 \\ 0 & Q_i \end{bmatrix} \quad [50]$$

$$h(t) = \begin{bmatrix} h_c(t) & 0 \\ 0 & h_i(t) \end{bmatrix} \quad [51]$$

where the subscript "*c*" is associated with modes that will be controlled and the subscript "*i*" corresponds to modes that will be ignored. The size of the zero components in the *Q* matrix is dependent on the number of modes to be controlled or ignored. If *n* modes are controlled and *m* modes are ignored, where $n + m = 6$, the entire system reduces to

$$\begin{bmatrix} \dot{\bar{\Gamma}}_{c(nx1)}(t) \\ \dot{\bar{\Gamma}}_{i(mx1)}(t) \end{bmatrix} = \begin{bmatrix} Q_{c(nxn)} + g_{c(nx3)}(t)w_{c(3xn)}(t) & g_{c(nx3)}(t)w_{i(3xm)}(t) \\ g_{i(mx3)}(t)w_{c(3xn)}(t) & Q_{i(mxm)} + g_{i(mx3)}(t)w_{i(3xm)}(t) \end{bmatrix} \times \begin{bmatrix} \bar{\Gamma}_{c(nx1)}(t) \\ \bar{\Gamma}_{i(mx1)}(t) \end{bmatrix} \quad [52]$$

$$\bar{\Psi}(t) = \begin{bmatrix} h_{c(nxn)} & 0_{nxm} \\ 0_{mxn} & h_{i(mxm)} \end{bmatrix} \begin{bmatrix} \bar{\Gamma}_{c(nx1)}(t) \\ \bar{\Gamma}_{i(mx1)}(t) \end{bmatrix} \quad [53]$$

Let $w_{i(3xm)}(t) = 0_{3xm}$ because it only affects ignorable modes, then equation [52] reduces to the following

$$\begin{bmatrix} \dot{\bar{\Gamma}}_{c(nx1)}(t) \\ \dot{\bar{\Gamma}}_{i(mx1)}(t) \end{bmatrix} = \begin{bmatrix} Q_{c(nxn)} + g_{c(nx3)}(t)w_{c(3xn)}(t) & 0_{nxm} \\ g_{i(mx3)}(t)w_{c(3xn)}(t) & Q_{i(mxm)} \end{bmatrix} \times \begin{bmatrix} \bar{\Gamma}_{c(nx1)}(t) \\ \bar{\Gamma}_{i(mx1)}(t) \end{bmatrix} \quad [54]$$

The state matrix is now upper diagonal. Define Q'_c as a matrix with desirable system eigenvalues and set it equal to the upper *n* x *n* block of the current state matrix,

$$Q'_{c(nxn)} = Q_{c(nxn)} + g_{c(nx3)}(t)w_{c(3xn)}(t) \quad [55]$$

The control is evaluated as

$$w_{c(3xn)}(t) = \left[g_{c(nx3)}(t)\right]^{-1}\left(Q'_{c(nxn)} - Q_{c(nxn)}\right) \quad [56]$$

Equation [56] will yield an exact solution if exactly three modes are controlled. If more or less than three modes

are controlled, equation [56] can generate a minimum norm solution or no solution. This follows from the fact that $g_{c(n\times 3)}(t)$ is only square (and invertible) when the dimensions of B_c are 3 x 3.

This example, with a focus on three modes, is notable as demonstrated by equations [34] and [35]. Assuming exactly three modes are removed, the control gain $\kappa(t)$ for use with [21] can be identified, i.e.,

$$w(t) = \kappa(t)E(t)S^{-1} \quad [59]$$

$$\left[g^{-1}_{c(3x3)}(t)\left(Q'_{c(3x3)} - Q_{c(3x3)}\right) \quad 0_{3x3}\right]SE(t)^{-1} = \kappa(t) \quad [60]$$

It is apparent from equation [54], that the function, $g_{i(m\times 3)}(t)w_{c(3\times n)}(t)$, is periodic. From the definition of *w(t)*,

$$g(t)w(t) = g(t)\kappa(t)E(t)S^{-1} \quad [61]$$

By substituting $\kappa(t)$ from equation [60],

$$g(t)w(t) = g(t)[g^{-1}_{c(3\times 3)}(Q'_{c(3\times 3)} - Q_{c(3\times 3)}) \quad 0_{3\times 3}] \quad [62]$$

and substituting the partitioned matrices *g(t)* and *w(t)* from equations [48] and [49] respectively,

$$\begin{bmatrix} g_{c(3x3)}(t)w_{c(3x3)}(t) & g_{c(3x3)}(t)w_{i(3x3)}(t) \\ g_{i(3x3)}(t)w_{c(3x3)}(t) & g_{i(3x3)}(t)w_{i(3x3)}(t) \end{bmatrix} = \begin{bmatrix} g_{c(3x3)}(t) \\ g_{i(3x3)}(t) \end{bmatrix}\left[g^{-1}_{c(3x3)}\left(Q'_{c(3x3)} - Q_{c(3x3)}\right) \quad 0_{3x3}\right] \quad [63]$$

Therefore,

$$g_{i(3x3)}(t)w_{c(3x3)}(t) = g_{i(3x3)}(t)g^{-1}_{c(3x3)}(t)\left(Q'_{c(3x3)} - Q_{c(3x3)}\right) \quad [64]$$

Because *g(t)* is periodic, ($g(t) = SE(t)^{-1}B$ and *E(T)* are periodic by definition), $g_{i(3x3)}(t)w_{c(3x3)}(t)$ is also periodic. Thus, the stability of the system matrix in equation [54] is determined by the eigenvalues of Q'_c and Q_i.

Since our linearized system includes four eigenvalues along the imaginary axis, one stable, as well as one unstable mode, the gain $\kappa(t)$ will not yield a system that is asymptotically stable. In other words, for equation [56] to result in an exact solution, exactly three modes must be modified. The system in equation [21] possesses five modes that are not asymptotically stable; therefore, the motion of the controlled system will be bounded relative to a nominal halo orbit, but not asymptotically approach it. If more than three modes are removed, the solution to equation [56] can be found via a minimum norm approximation. However, the stability of such a solution is not approached analytically here. In the case of interferometric imaging arrays, bounded motion creates more favorable (*u*, *v*) plane coverage.

This continuous algorithm allows the eigenvalues of matrix Q_c to be shifted to desired locations. If the eigenvalues of Q'_c are selected to equal the eigenvalues of Q_i, the impulsive maneuvers in equations [34] and [35] can be reproduced continuously and the resulting motion is bounded in the linear system. Other bounded solutions are also available when the eigenvalues of Q'_c are selected to be stable but not equal to those of Q_i.

Stability of Controlled Nonlinear System

Because the control ($\Delta\bar{v}_{3x3}$) is determined using linearized variational equations (representing perturbations), the stability of the feedback controller applied in the nonlinear system is difficult to assess analytically. The algorithm is implemented (in state space form) as follows,

$$\dot{x}_1 = x_2 + \Delta v_x \quad [65]$$

$$\dot{x}_2 = 2(x_4 + \Delta v_y) + x_1 - \cdots - \frac{(1-\mu_G)(x_1+\mu_G)}{R_1^3} - \frac{\mu_G(x_1-(1-\mu_G))}{R_2^3} \quad [66]$$

$$\dot{x}_3 = x_4 + \Delta v_y \quad [67]$$

$$\dot{x}_4 = -2(x_2 + \Delta v_x) + x_3 - \cdots - \frac{(1-\mu_G)x_3}{R_1^3} - \frac{\mu_G x_3}{R_2^3} \quad [68]$$

$$\dot{x}_5 = x_6 + \Delta v_z \quad [69]$$

$$\dot{x}_6 = -\frac{(1-\mu_G)x_5}{R_1^3} - \frac{\mu_G x_5}{R_2^3} \quad [70]$$

where $\Delta\bar{v}_{3x1} = \begin{bmatrix} \Delta v_x \\ \Delta v_y \\ \Delta v_z \end{bmatrix}$ is determined from the gain $\kappa(t)$,

$x_1 = x$, $x_2 = \dot{x}$, $x_3 = y$, $x_4 = \dot{y}$, $x_5 = z$, $x_6 = \dot{z}$ and

$$R_1 = \left((x_1+\mu_G)^2 + x_3^2 + x_5^2\right)^{1/2} \quad [71]$$

$$R_2 = \left((x_1-(1-\mu_G))^2 + x_3^2 + x_5^2\right)^{1/2} \quad [72]$$

When the control as derived in the linear system is simulated in the nonlinear system, the spacecraft trajectories remain bounded relative to a nominal halo orbit over extended periods of time. The distance of a satellite relative to a Sun-Earth/Moon L2 orbit over approximately forty years (or 80 halo orbit periods) appears in Figure 6.1. The motion is periodic and bounded. The satellite is initially placed 1.25 km away from the libration point orbit, shown in the upper left corner of Figure 6.2. The initial velocity of the satellite is equal to the velocity of the corresponding point on the halo orbit, labeled "L2," in the same figure. Figure 6.2 also illustrates the motion of the satellite over the course of approximately 40 years. This motion is in an inertial frame, relative to the L2 halo orbit and appears in three inertial projections: *y*-*z*, *x*-*y*, and *x*-*z*. The satellite is controlled via the continuous Floquet controller, with Q'_c selected such that $eig(Q'_c) = eig(Q_i)$ and the eigenvalues of Q_i are the stable mode and the two short period center modes of *Q*.

FORMATION SIMULATION AND IMAGE RECONSTRUCTION

A number of assumptions are incorporated into the image reconstruction methodology. First, the image is modeled as fixed, i.e., it remains unchanged throughout the measurement period of 180 days. The interferometer is considered perfect; no noise is present in the measurement of the mutual coherence function and no starlight nulling is necessary. The satellite formation processes one measurement once every 1.8 days. The object of interest is assumed to be stationary and located in the inertial *x*-direction from the formation. The "true image" is considered to be the picture of Jupiter in Figure 2.

Example 1: Short Baseline, Five Satellite Formation

By appropriate choice of Q_c', natural, nearly periodic motions in the phase space can be exploited that are particularly advantageous to interferometric arrays. These solutions offer adequate, repeated coverage of the (*u*, *v*) plane in a desired direction as well as controlled motion in physical space. The motion of a short baseline (5 km) formation moving near the Sun-Earth/Moon L2 point appears in Figures 7.1 and 7.2. The formation is used to construct an image of a Jupiter-like planet (Figure 2) located 4.2 million light years from Earth (a planet near our closest star, Alpha Centauri) at a wavelength of 500 nm (visible blue light). The corresponding coverage of the (*u*, *v*) plane and simulated image reconstruction appear in Figure 8.

This type of formation could be compared with the planned interferometric imaging mission, Terrestrial Planet Finder (TPF).[1] The TPF mission attempts to identify Earth-like planets in other solar systems. The nominal mission design includes five satellites flying in precise formation; a physical combination of interferometric beams is required to locate exosolar planets. Several levels of control are necessary to coordinate the position of active optics to nanometer accuracy. Although the motion of this example array is advantageous to optical imaging, much tighter control and coordination, perhaps in conjunction with a strategy similar to the described control method, would be required for the TPF mission.

The five satellites in the short baseline formation are initially placed in the configuration that appears in the upper left corner of Figure 7.1 (in the inertial frame.) The initial velocities of the satellites are all equal to the velocity of the corresponding point on the halo orbit, labeled "L2," in the same figure. Figure 7.1 also illustrates the motion of the short baseline formation over the course of one halo orbit period, or approximately 180 days. This motion is visible in an inertial frame, relative to the L2 halo orbit and projected onto three inertial planes: *y*-*z*, *x*-*y*, and *x*-*z*. Figure 7.2 displays the formation motion in Figure 7.1 in a three-dimensional plot.

Satellites 1, 2, 4, and 5 (as labeled in Figure 7.1) are controlled via the continuous Floquet controller, with Q_c' selected such that $eig(Q_c') = eig(Q_i)$ and the eigenvalues of Q_i are the stable mode and two short period center modes of Q. Satellite 3 is controlled to an unnatural nominal path. This trajectory is defined as stationary relative to the L2 orbit in the inertial frame. Satellite 3 is controlled using feedback linearization methods previously implemented and described by Howell and Marchand.[13]

Figure 8 demonstrates the resulting (*u*, *v*) coverage and image reconstruction of the "distant planet." In this example, the planet is placed in the inertial *x*-direction; therefore, the motion in a plane perpendicular to the direction of the object of interest is constrained to the inertial *y*-*z* plane. The selection of the location of the object of interest is arbitrary. The bottom line of Figure 8 illustrates motion of the formation in the inertial *y*-*z* direction at four times during the 180 day period. Each square represents the location of a satellite in physical space corresponding to four different times at which a measurement of the mutual coherence function is obtained. Along the middle line of Figure 8 is the corresponding (*u*, *v*) plane coverage at each of the four times. Each circle represents a point on the (*u*, *v*) plane where the mutual coherence function is measured. Finally, the top line of Figure 8 represents the image reconstruction as time progresses.

The control effort required to maintain satellites 1, 2, 4, and 5 in the short baseline formation appears in Figure 9. This control effort is plotted over two periods of the libration point orbit. It is interesting to note that the required control is nearly periodic. Also, the amount of control required to maintain satellites 1 and 5 in the short baseline formation is approximately twice that required for satellites 2 and 4.

Example 2: Long Baseline, 16 Satellite Formation

With a critical set of values for the elements of the matrix Q_c', natural solutions in the phase space relative to the halo orbit emerge that maintain a 16 satellite formation bounded within a maximum baseline requirement over long periods of time. These solutions create quasi-randomly distributed satellites in many look-directions, as evident in Figures 10.1 and 10.2. But, throughout the simulation, the satellites do not collide. Since the natural formation motion is quasi-periodic (as in Figure 6) the satellites are not likely to collide for extended periods of time. The formation is imaging an object located at 1AU from the Earth at 7MHz (AM radio wavelengths.)

This type of formation can be compared with the planned Solar Imaging Radio Array (SIRA) mission. One of the goals of the SIRA mission is to perform low-frequency radio imaging of the Sun to determine the dynamics and interaction of coronal mass ejections.[3] The nominal mission design includes 16 satellites, initially arranged on a sphere, with a maximum baseline of between 5 and 25 km. The SIRA mission must maintain adequate coverage of the (*u*, *v*) plane in all look-directions at all times for radio waves with frequencies between 30 kHz and 15 MHz. If a quasi-random distribution of satellites is maintained in SIRA, coverage of the (*u*, *v*) plane is adequate for many mission science goals.[36] The SIRA mission may not require substantial control beyond that described here.

The 16 satellites in the long baseline formation are initially placed on a spiral around a sphere as seen in the upper left corner of Figure 10.1 (in the inertial frame.) This initial configuration is being considered for the SIRA mission.[37] As in the previous example, the initial velocities of the satellites are all equal to the velocity of the corresponding point on the halo orbit, labeled "L2," in the same figure. Figure 10.1 also illustrates the motion of the long baseline formation over the course of one halo orbit period, or approximately 180 days. This motion remains bounded within the sphere and maintains a quasi-random distribution of satellites over the time. Figure 10.2 displays the formation motion in Figure 10.1 on a three-dimensional plot.

The (u, v) coverage and image reconstruction of an object located at 1AU from the Earth is demonstrated in Figure 11. In this example, the "planet" is again placed in the inertial x-direction. As in Figure 9, the bottom line of Figure 11 illustrates motion of the formation in the inertial y-z direction at four times during the 180 day period. Each square represents the location of a satellite in physical space at the instant that corresponds to measurement of the mutual coherence function. The middle line in Figure 11 is the corresponding (u, v) plane coverage and the top line of Figure 11 reflects image reconstruction as time progresses.

SUMMARY AND CONCLUDING REMARKS

In the present study, a continuous control algorithm is developed that facilitates bounded motion of satellite formations over long periods of time near halo orbits in the circular restricted three-body problem (CR3BP). The feedback controller is designed based on the linear variational equations. Through simulation, the linear controller is demonstrated to be effective using the full nonlinear CR3BP equations of motion. By changing certain parameters within the control algorithm, trajectories that are particularly advantageous to satellite imaging formations emerge. Image reconstruction and coverage of the (u, v) plane are simulated for interferometric satellite configurations, demonstrating potential applications of the control algorithm and resulting motion.

Motion advantageous to imaging arrays can be produced via more traditional control methods, where a desired unnatural trajectory is strictly followed. However, such approaches sometimes ignore multi-body dynamics or simply remove them using control methods such as feedback linearization. By including multi-body dynamics in the development of the control algorithm, natural motions in the multi-body regime are exploited and potentially reduce required control effort. Some formations that do not require tight control, such as the configuration proposed in SIRA, potentially benefit.

Future work includes testing of the control algorithm in a more complete ephemeris model as well as analytically evaluating stability of the algorithm in the nonlinear system with disturbances. A more realistic image reconstruction model (including measurement noise and motion of the object of interest) can also be investigated.

ACKNOWLEDGEMENTS

The authors would like to thank Zubin Olikara for modeling the formation motion in three dimensions (used in the associated conference presentation). This work was performed at Purdue University with support from NASA Goddard Space Flight Center under contract numbers NCC5-727 and NNG04GP69G.

REFERENCES

[1] TPF Science Working Group. Terrestrial Planet Finder: A NASA Origins Program to Search for Habitable Planets, 1999.

[2] Gendreau, K.C., W.C. Cash, A.F. Shipley, and N. White, "The MAXIM Pathfinder X-ray Interferometry Mission," Proceedings of the the International Society for Optical Engineering (SPIE) Conference, Waikoloa, Hawaii, August 26-28, 2002.

[3] MacDowall, R., M. Kaiser, N. Gopalswamy, "Solar Imaging Radio Array (SIRA): Radio Aperture Synthesis from Space," 34th AAS Solar Physics Division Meeting, May 2003, Vol. 23, pp. 20-22.

[4] Scharf, Daniel P., Fred Y. Hadaegh, and Scott R. Ploen, "A Survey of Spacecraft Formation Flying Guidance and Control (Part I): Guidance," American Control Conference, Denver, Colorado, June 4-6, 2003.

[5] Scharf, Daniel P., Fred Y. Hadaegh, and Scott R. Ploen, "A Survey of Spacecraft Formation Flying Guidance and Control (Part II): Control," American Control Conference, Boston, Massachusetts, June 30-July 2, 2004.

[6] Gurfil, P. and N. J. Kasdin, "Dynamics and Control of Spacecraft Formation Flying in Three-Body Trajectories," AIAA Guidance, Navigation, and Control Conference and Exhibit, Montreal, Canada, August 6-9, 2001. AIAA Paper 2001-4026.

[7] Gurfil, P., M. Idan, and N.J. Kasdin, "Adaptive Neural Control of Deep-Space Formation Flying," American Control Conference (ACC) Proceedings, Anchorage, Alaska, Vol. 4, May 8-10, 2002, pp. 2842-2847.

[8] Luquette, R.J. and R. M. Sanner, "A Non-Linear Approach to Spacecraft Formation Control in the Vicinity of a Collinear Libration Point." AAS/AIAA Astrodynamics Conference; Proceedings, Quebec, July 30 – August 2, 2001, pp. 437-445.

[9] Hamilton, N.H., Formation Flying Satellite Control Around the L2 Sun-Earth Libration Point, M.S. Thesis, George Washington University, Washington, DC, December 2002.

[10] Folta, D., J.R. Carpenter, and C. Wagner, "Formation Flying with Decentralized Control in Libration Point Orbits," International Symposium: Spaceflight Dynamics, Biarritz, France, June 2000.

[11] Gómez, G., K.C. Howell, J. Masdemont, and C. Simó, "Station-keeping Strategies for Translunar Libration Point Orbits," *Advances in Astronautical Sciences*, Vol. 99, Pt.2, 1998, pp. 949-967.

[12] Gómez, G., M. Lo, J. Masdemont, and K. Museth, "Simulation of Formation Flight Near Lagrange Points for the TPF Mission," AAS/AIAA Astrodynamics Conference, Quebec, Canada, July 30 – August 2, 2001, AAS Paper 01-305.

[13] Howell, K.C. and B.G. Marchand, "Control Strategies for Formation Flight in the Vicinity of the Libration Points," AIAA/AAS Space Flight Mechanics Conference, Ponce, Puerto Rico, February 9-13, 2003, AAS Paper 03-113.

[14] Marchand, B.G. and K.C. Howell, "Aspherical Formations Near the Libration Points in the Sun-Earth/Moon Ephemeris System," 2004 AAS/AIAA Spaceflight Mechanics Conference, Maui, Hawaii, February 8-11, 2004, AAS Paper 04-157.

[15] Barden, B. T. and K.C. Howell, "Fundamental Motions Near Collinear Libration Points and Their Transitions," *The Journal of the Astronautical Sciences*, Vol. 46, No. 4, 1998, pp. 361-378.
[16] Barden, B. T. and K.C. Howell, "Formation Flying in the Vicinity of Libration Point Orbits," *Advances in Astronautical Sciences*, Vol. 99, Pt. 2, 1998, pp. 969-988.
[17] Howell, K.C. and B. T. Barden, "Trajectory Design and Stationkeeping for Multiple Spacecraft in Formation Near the Sun-Earth L1 Point," IAF, 50th International Astronautical Congress, Amsterdam, Netherlands, Oct. 4-8, 1999. IAF/AIAA Paper 99-A707.
[18] Barden, B.T. and K.C. Howell, "Dynamical Issues Associated with Relative Configurations of Multiple Spacecraft Near the Sun-Earth/Moon L1 Point," AAS/AIAA Astrodynamics Specialist Conference, Girdwood, Alaska, August 16-19, 1999, AAS Paper 99-450.
[19] Marchand, B. G. and K.C. Howell, "Formation Flight Near L1 and L2 in the Sun-Earth/Moon Ephemeris System Including Solar Radiation Pressure," AAS/AIAA Astrodynamics Specialist Conference, Big Sky, Montana, August 3-8, 2003. AAS Paper 03-596.
[20]Chakravorty, S., Design and Optimal Control of Multi-Spacecraft Interferometrc Imaging Systems, Ph.D. Thesis, University of Michigan, 2004.
[21] Born, M. and E. Wolf. Principles of Optics. Pergamon Press, New York, New York, 1964.
[22] Hyland, D.C., "Interferometric Imaging Concepts with Reduced Formation-Keeping Constraints," AIAA Space 2001 Conference, Albuquerque, New Mexico, August 2001.
[23] Hyland, D.C., "The Inverse Huygens-Fesnel Principle and It's Implications for Interferometric Imaging," *The Journal of Astronautical Sciences*, 2003.
[24] Hussein, I.I., D.J. Scheeres, and D.C. Hyland, "Formation Path Planning for Optimal Fuel and Image Quality for A Class of Interferometric Imaging Missions," February 2003, AAS Paper 03-172.
[25]Hussein, Islam I., Daniel J. Scheeres, and David C. Hyland, "Control of a Satellite Formation For Imaging Applications," Proceedings of the American Control Conference, 2003, pp. 308-313.
[26] Hussein, I.I., D.J. Scheeres, and David C. Hyland, "Optimal Formation Control for Imaging and Fuel Usage," 15th AAS/AIAA Space Flight Mechanics Conference, Copper Mountain, Colorado, January 23-27, 2005. AAS Paper 05-160.
[27] Hussein, I.I., Daniel J. Scheeres, and David C. Hyland, "Optimal Formation Control for Imaging and Fuel Usage with Terminal Imaging Constraints," IEEE Conference on Control Applications, 2005.
[28] Hussein, Islam I. and Anthony M. Bloch, "Dynamic Coverage Optimal Control for Interferometric Imaging Spacecraft Formations," 43rd IEEE Conference on Decision and Control, Paradise Island, Bahamas, December 2004, pp.1812-1817.
[29] Hussein, Islam, I. and Anthony M. Bloch, "Dynamic Coverage Optimal Control for Interferometric Imaging Spacecraft Formations (Part II): The Nonlinear Case," Proceedings of the American Control Conference, 2005, pp. 2391-2396.
[30] Folland, Gerald B., Fourier Analysis and It's Applications, Brooks/Cole Publishing Company, Pacific Grove, California, 1992.
[31] Joshi, S.S., "An Informal Introduction to Synthetic Aperture Imaging," JPL Interoffice Memorandum 3450-98-0004, January 12, 1998, pp. 1-16.
[32] Howell, K. C. and T. M. Keeter, "Station-Keeping Strategies for Libration Point Orbits: Target Point and Floquet Mode Approaches," AAS/AIAA Spaceflight Mechanics Meeting, Albuquerque, New Mexico, February 13-16, 1995.
[33] Wiesel, W. and W. Shelton, "Modal Control of an Unstable Periodic Orbit," *The Journal of the Astronautical Sciences*, Vol. 31, March 1983, pp.63-76.
[34] Poincaré, H., Les Methodes Nouvelles de la Mechanique Celeste, Dover, New York, 1957.
[35] Szebehely, V., Theory of Orbits Academic Press, New York, 1967.
[36] MacDowall, R., "SIRA : Uniform Distributions in the (u,v) Aperture Plane," Presentation, NASA Goddard Space Flight Center, October 3, 2005.
[37] Folta, Dave, Bo Naasz, and Frank Vaughn, "Solar Imaging Radio Array (SIRA) Trajectory and Formation Analysis," Presentation, Dynamics Analysis Branch, NASA Goddard Space Flight Center, January 30, 2003.

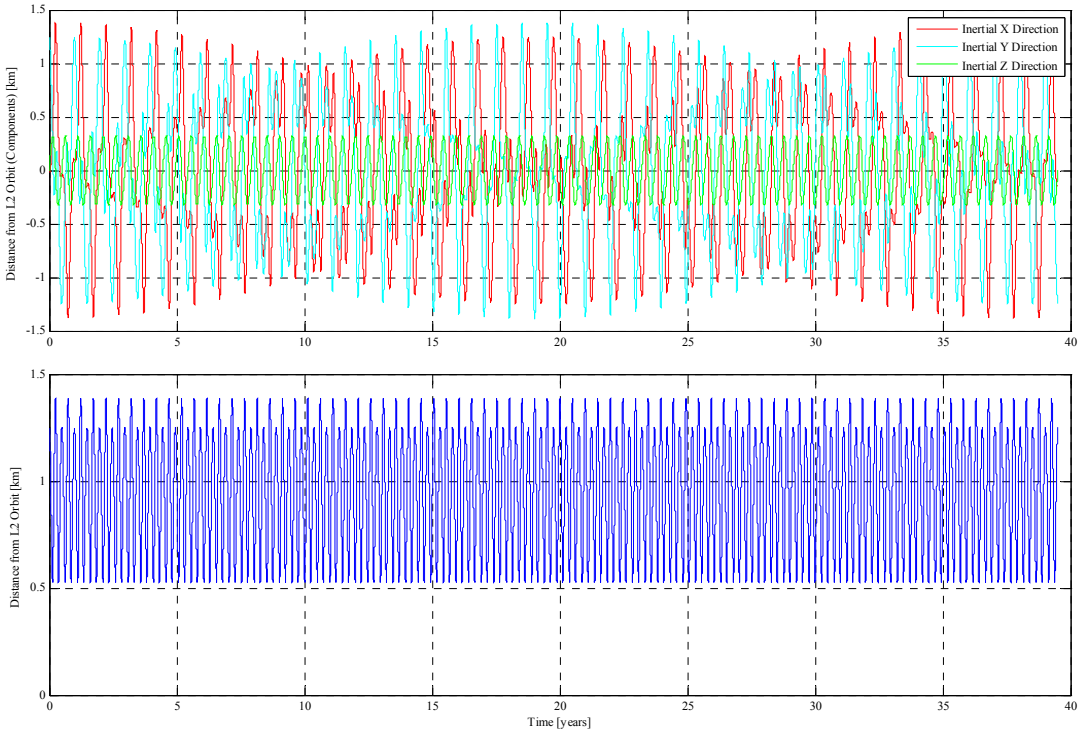

Figure 6.1: Distance of Satellite from L2 (Sun-Earth/Moon) Orbit with Floquet Control

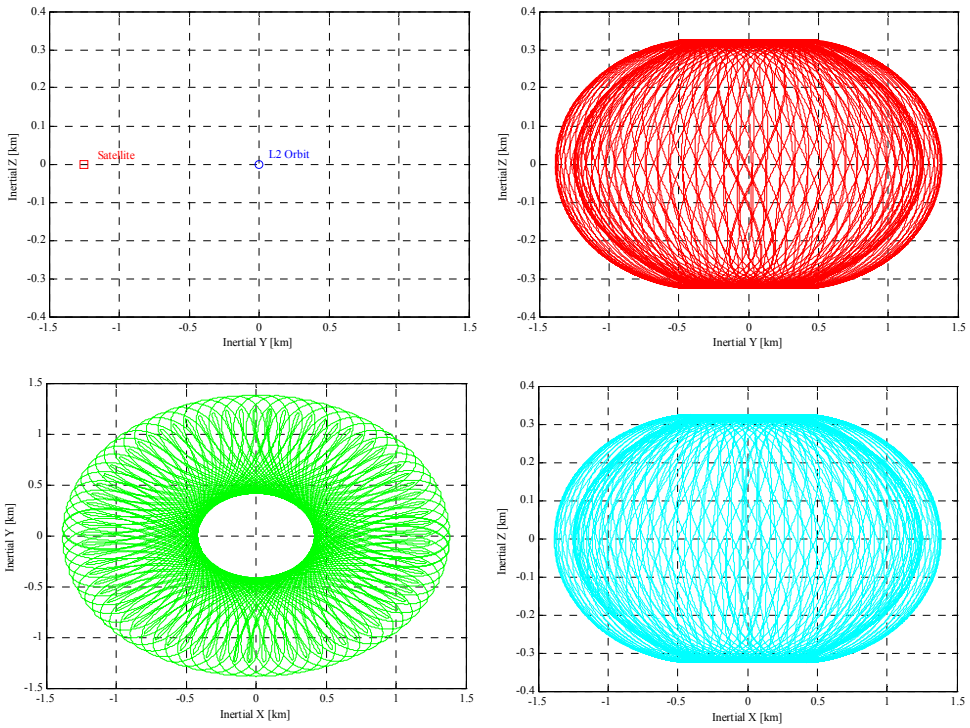

Figure 6.2: Bounded, Quasi-Periodic Motion of Satellite Relative to L2 (Sun-Earth/Moon) Orbit with Floquet Control

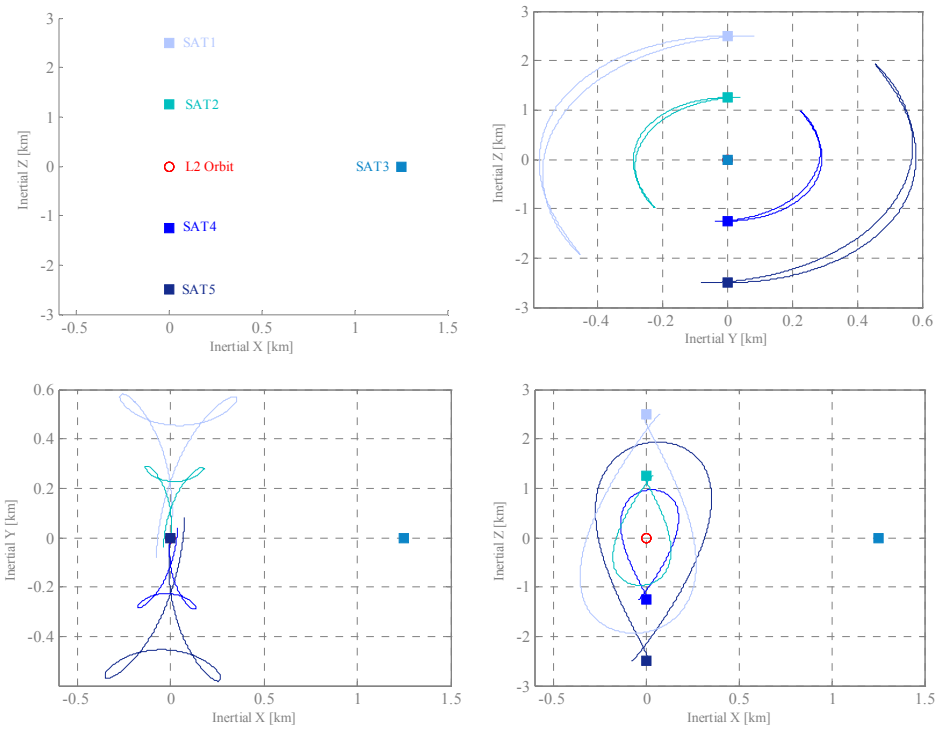

Figure 7.1: Short Baseline Formation Motion Relative to Sun-Earth L2 Orbit (Approximately One Period or 180 days)

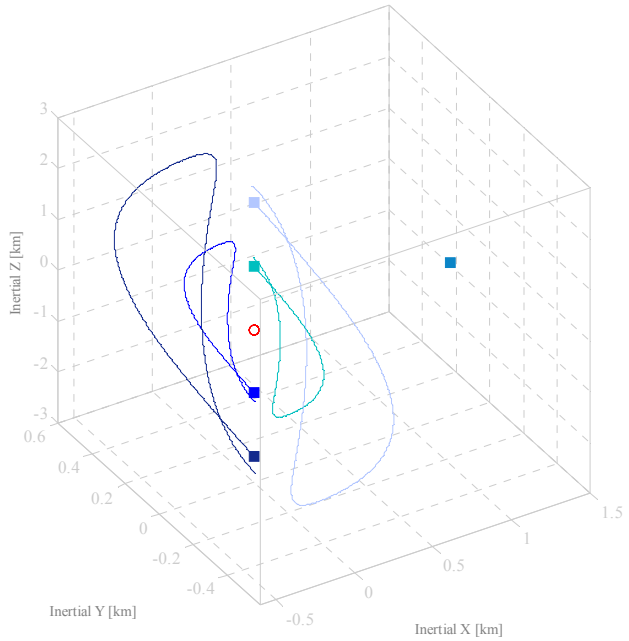

Figure 7.2: Short Baseline Formation Three-Dimensional Motion Relative to Sun-Earth L2 Orbit (Approximately One Period or 180 days)

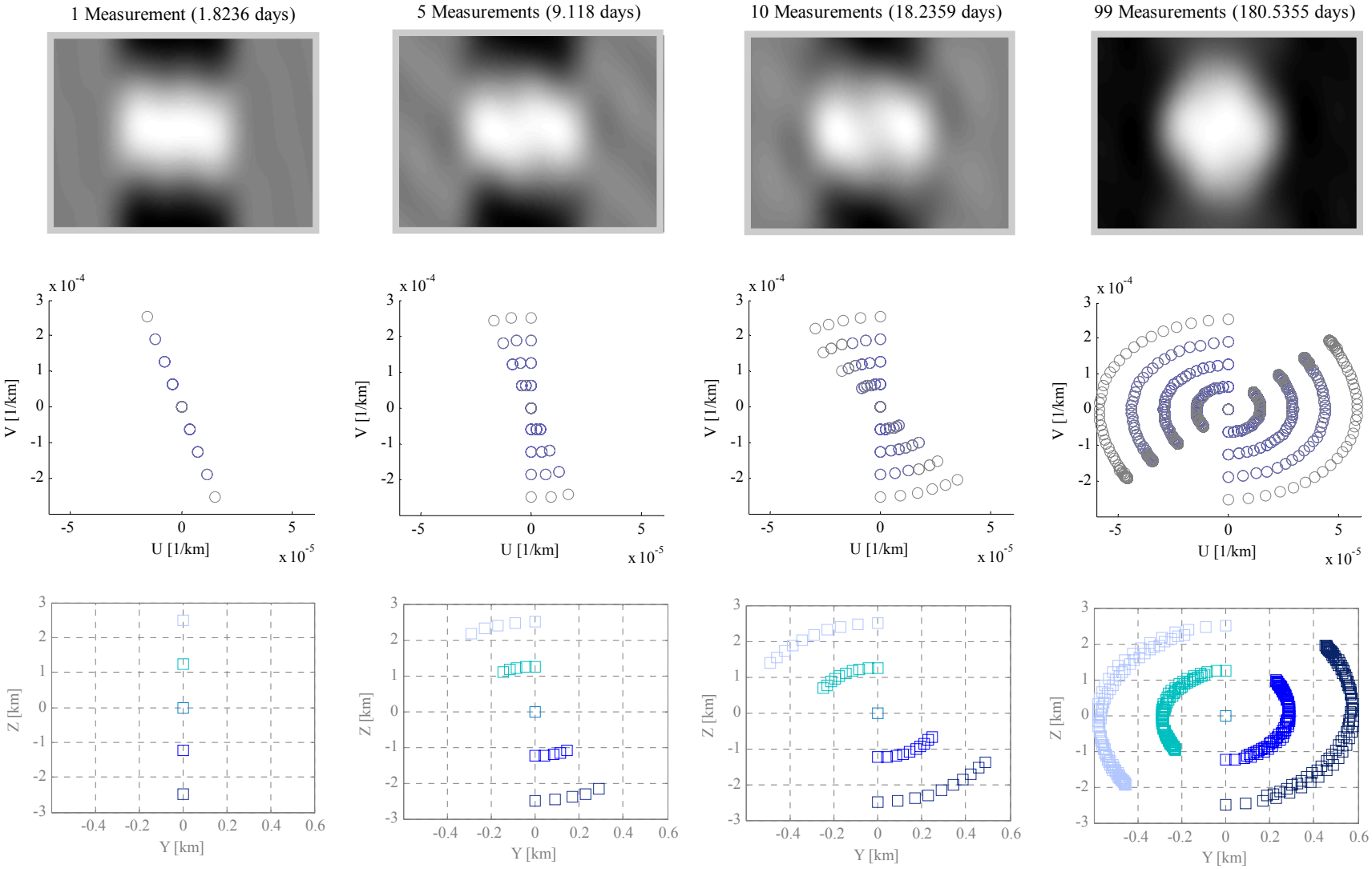

Figure 8: Image Reconstruction via Short Baseline Formation

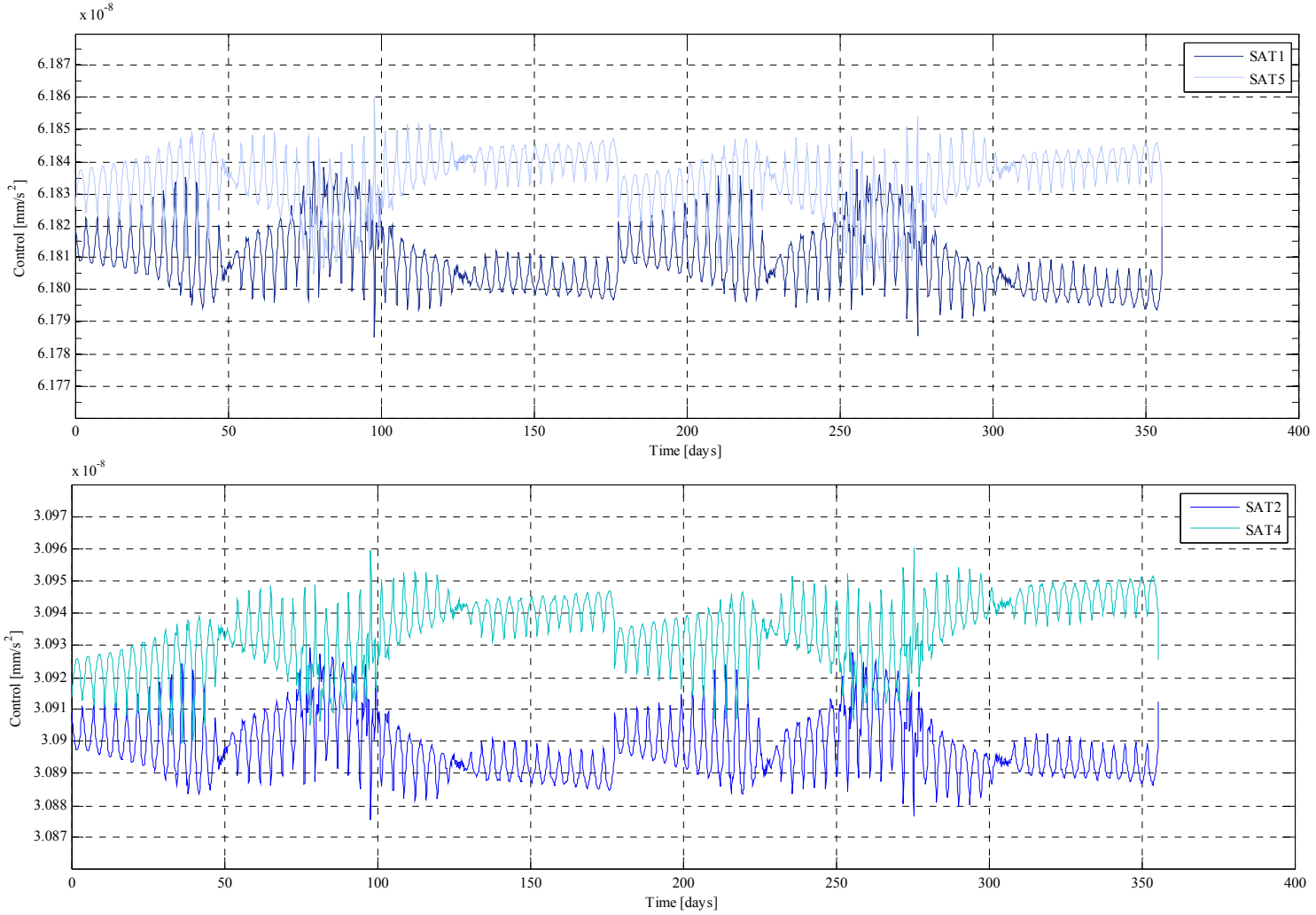

Figure 9: Total Control Required for Short Baseline Formation (Two Halo Orbit Periods, or Approximately 360 Days)

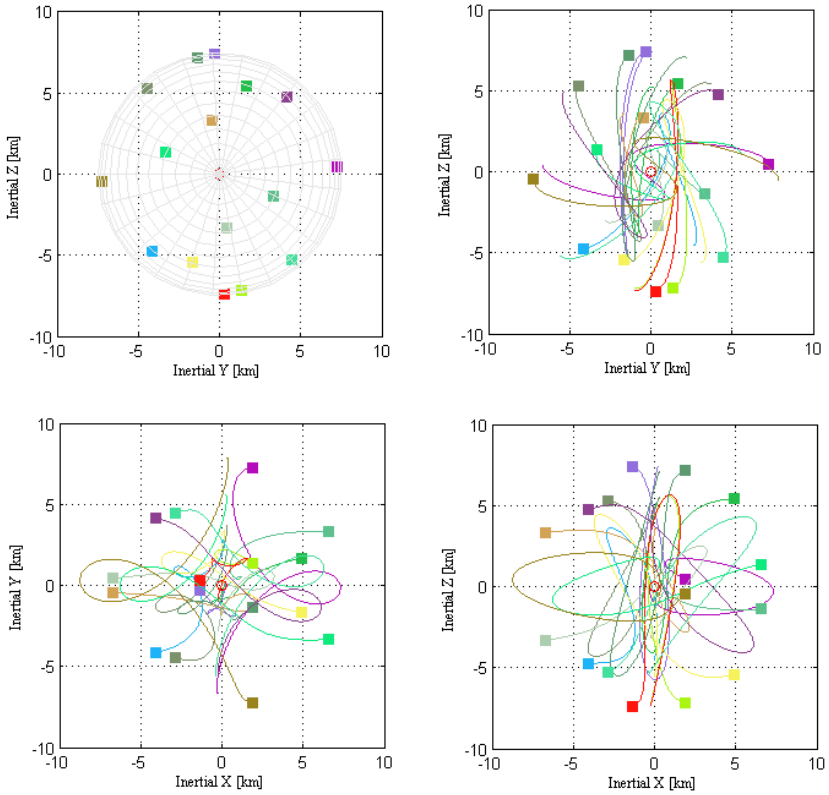

Figure 10.1: Long Baseline Formation Motion Relative to Sun-Earth L2 Orbit (Approximately One Period or 180 days)

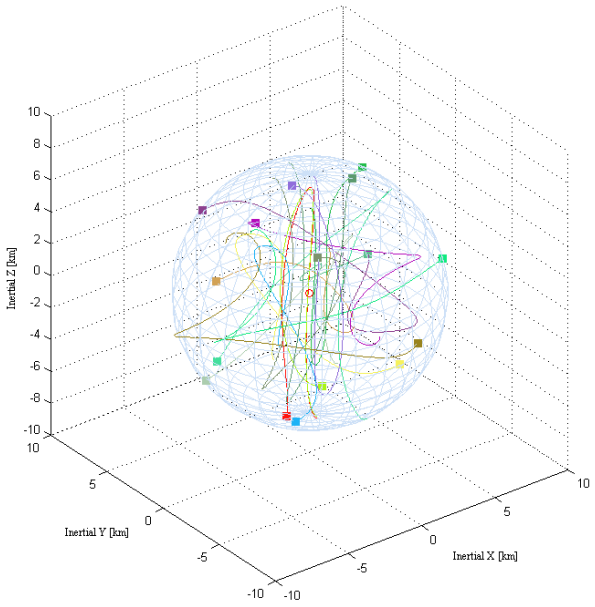

Figure 10.2: Long Baseline Formation Three-Dimensional Motion Relative to Sun-Earth L2 Orbit (Approximately One Period or 180 days)

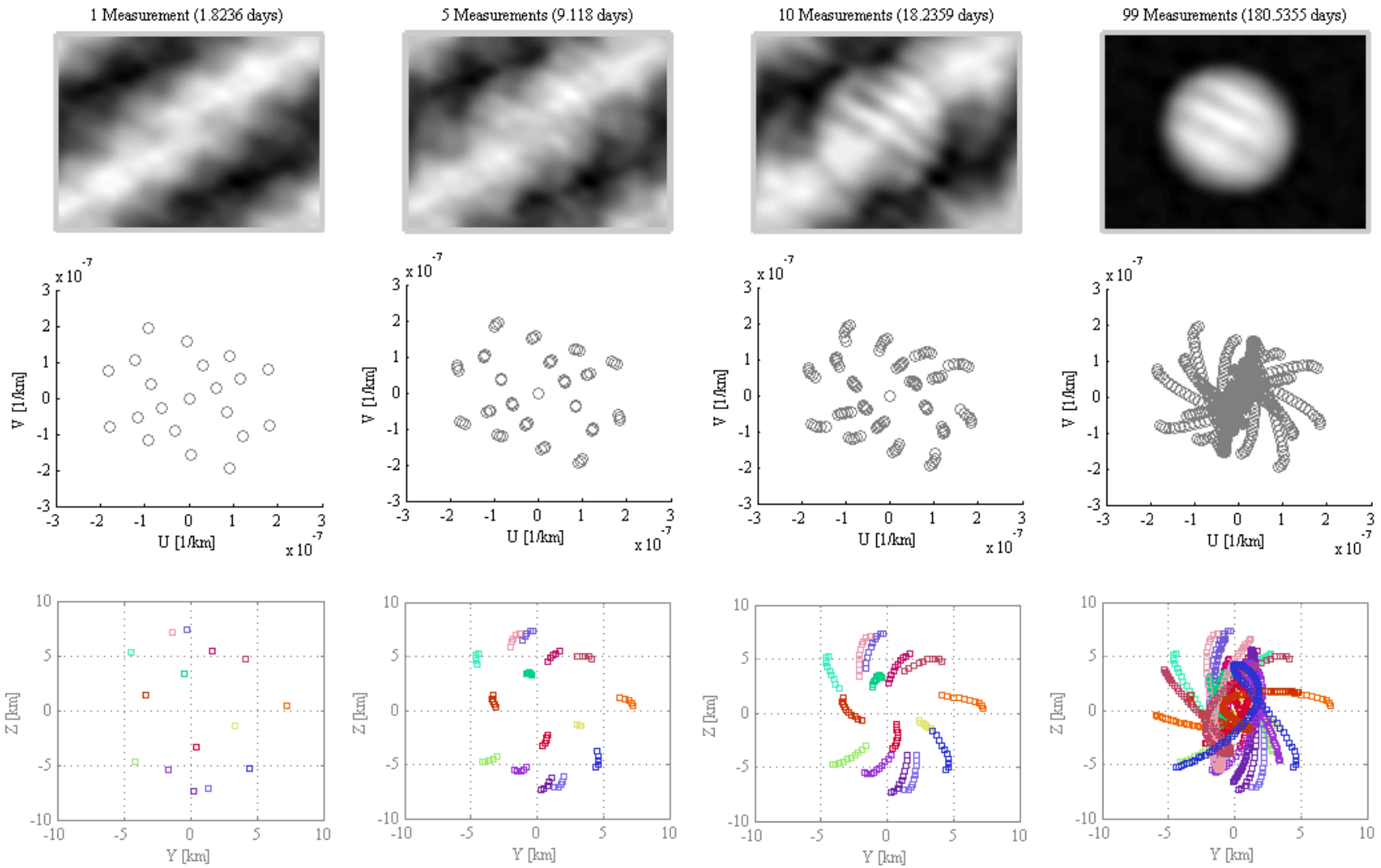

Figure 11: Image Reconstruction via Long Baseline Formation